On the selection of an empirical material constitutive model for the finite element modeling of Ti6Al4V orthogonal cutting, including the segmented chip formation

F. Ducobu[1] · P.-J. Arrazola[2] · E. Rivière-Lorphèvre[1] · E. Filippi[1]

Abstract

Finite element modeling of machining aims for guidance in the choice of the cutting parameters and for the comprehension of the involved phenomena. The modeling of the behavior of the machined material is a key parameter to develop a realistic model. It is nowadays still extremely difficult to acquire experimental data on the material flow stress due to the extreme conditions encountered during machining. Many constitutive models are found in the literature and there is a lack of objective information to choose the best suited for a given application. Four empirical constitutive models are used in this paper to represent the *Ti6Al4V* titanium alloy during an orthogonal cutting operation. All of them are based on the well-known Johnson-Cook model. The results of this study show that the influence of the constitutive model on the chip morphology and on the cutting force is high and that the strain softening phenomenon should be taken into account to produce a segmented (or saw-toothed) chip as it is experimentally observed. For the cutting conditions adopted, adding damage properties in the chip is moreover required to obtain a morphology close to the experimental reference. All these elements allow to get a reliable numerical model able to reproduce cutting forces and chip morphology (either continuous or segmented) for various cutting conditions.

Keywords Constitutive model · Chip formation · Experiments · Finite element · Orthogonal cutting · Titanium alloy Ti6Al4V

Introduction

The high mechanical, fatigue and corrosion resistances of *Ti6Al4V* titanium alloy, coupled with a low density and a good biocompatibility lead to an increase of its use in the aerospace and biomedical fields as machined parts [1]. It is however a hard-to-machine material due to its low thermal conductivity coupled with hardening. Finite element modeling can enhance the comprehension of the phenomena involved in machining. It is also intended to help the practitioner in the choice of the adequate cutting parameters. The development of realistic finite element models requires to model correctly the machined material in extreme conditions of strain, strain rate and temperature. These extreme conditions can, however, not be reached by current experimental means of tests. Indeed, today's experimental technology does not allow to reach sufficiently high strains and strain rates, moreover at high temperatures except for machining test itself. For example, Lee and Lin [2] provide experimental curves for strains up to 0.25 and strain rates of 2000 s^{-1} at temperatures between 973 K and 1373 K, rather low values in modeling of machining for which strains up to 6 can be reached, as well as strain rates of 10E7 s^{-1} and rate of temperature gradient of the order of 10E6 K/s when crossing the primary shear zone [3]. The material constitutive models developed based on these tests therefore only represent partially the material behavior in the conditions of the cutting process. The limitations of these constitutive models (currently mostly emprirical models) are particularly observed for the Johnson-Cook model [4], although it is the most used in the field (and consequently also for *Ti6Al4V*, the machined material considered in this work).

✉ F. Ducobu
Francois.Ducobu@umons.ac.be

1   Faculty of Engineering (FPMs), Machine Design and Production Engineering Lab, University of Mons (UMONS), 20 Place du Parc, B-7000 Mons, Belgium

2   Faculty of Engineering, Mechanical and Manufacturing Department, Mondragon University, Mondragon, Spain

In order to solve this issue, several empirical constitutive models have been introduced recently [4–8]. They, among others, take into account the strain softening, contributing to the formation of segmented (or saw-toothed) *Ti6Al4V* chip [4, 9]. The parameters of these constitutive models are usually obtained through inverse analysis thanks to the observation of the experimental chips global morphology, their geometrical characteristics and the measured cutting forces. In the end, the user misses objective arguments to choose between these constitutive models in the absence of experimental reference curves due to the practical limits mentioned earlier. Moreover, few comparisons between the results when using different constitutive models are available in the literature [10–12].

To fill this gap, this article compares four constitutive models based on the well-known Johnson-Cook flow stress model by introducing them in a finite element model for, in a first time, cutting conditions leading to a segmented chip, the hardest morphology to model. The results are then opposed to an experimental reference obtained in strictly orthogonal cutting conditions in order to highlight the differences they lead to and to provide objective information to choose which flow stress should be adopted for future modeling. The comparison is divided in two steps: firstly, no damage properties are given to the chip to allow the strict comparison of the four flow stresses. Secondly, damage is added in the chip to obtain more realistic morphologies and take the experimental observations during chip formation into account. The experimental – numerical comparison is focused on the data that are the most used and measured in practice: the chip morphology and the cutting force. In a second time, the cutting conditions are changed to provide continuous chips. The numerical results are compared to the experimental reference to show that the same model is able to predict the difference in the chip formation.

Table 1 Chemical composition in weight percent of *Ti6Al4V* grade 5 (ASM 4928) [15]

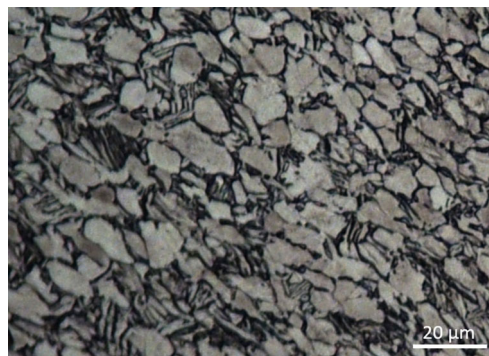| Element	Weight percent (%)
Al	5.5-6.75
C	≤ 0.08
Fe	≤ 0.4
H	≤ 0.015
N	≤ 0.03
O	≤ 0.2
Ti	87.725-91
V	3.5-4.5
Others, each	≤ 0.03
Others, total	≤ 0.05

Fig. 1 Microstructure of the base material

Experimental reference

The results from the experimental orthogonal cutting tests introduced in Ducobu et al. [13] were adopted to have an experimental reference in strictly orthogonal cutting and in the same cutting conditions as the numerical model. Titanium alloy *Ti6Al4V* grade 5 (ASM 4928, chemical composition in Table 1) at the classic state used in the aerospace industry (annealed at 750 °C for one hour followed by air cooling) was adopted for the experiments. The microstructure of the base material is provided in Fig. 1. The setup used a standard milling machine as a planning machine [13]. The machined sample is inserted into the
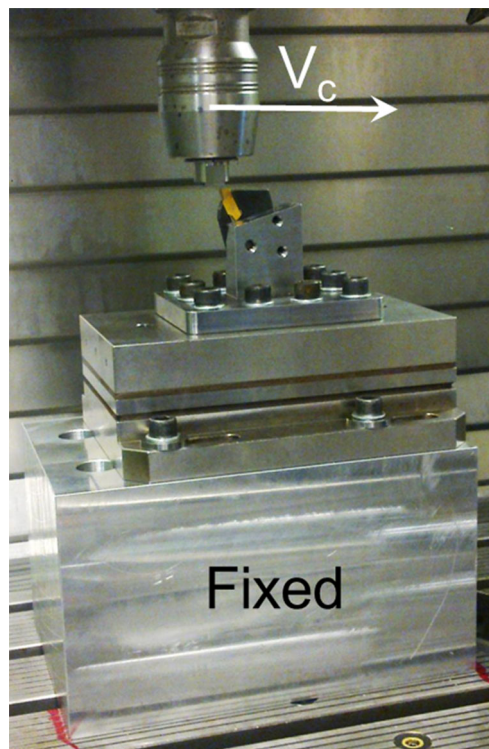

Fig. 2 Orthogonal cutting configuration on the milling machine [13]

spindle and the tool is fixed with a custom made support part on the force sensor, itself on the machine table. The cutting movement is the sample horizontal displacement with respect to the stationary tool (Fig. 2). This leads to the removal of a layer of material of constant and user-defined thickness in strictly orthogonal cutting conditions. In this configuration, the maximal achievable cutting speed is set by the maximal feed rate of the milling machine; typically of the order of 20 m/min to 30 m/min. The cutting length and the width of cut are set by the dimensions of the feature to machine, a 10 mm long and 1 mm wide tenon [13]. This cutting length is large enough for the process to be steady and the forces to be measured, while it is short enough to prevent the chip to roll up [13]. The chips can therefore be embedded without unrolling, and there is no error on the measured lengths due to the unrolling distortions. A width of 1 mm minimizes the efforts in the spindle bearings and it directly gives the forces value per mm width as in 2D plane strain numerical models (with a width of cut by uncut chip thickness ratio larger than 3 for the adopted values, to respect plane strain assumptions). The rake angle is 15°, the clearance angle 2° and the cutting edge radius 10 μm. The cutting speed is fixed at 30 m/min (i.e. the maximum feed rate of the machine). Four different uncut chip thickness values are adopted (Table 2): $h = 280$ μm (6 repetitions in the experiments) leads to a segmented chip, while $h = 40$ μm, 60 μm and 100 μm (3 repetitions in the experiments) lead to a continuous chip. Although the cutting speed also influences the chip formation and its morphology [14], only the uncut chip thickness varies in this study. Indeed, the experimental setup limits the maximum cutting speed to the maximum feed rate of the machine (30 m/min in this case), which does not allow to modify significantly the cutting speed while keeping it in an industry relevant range.

Numerical model

General features

The numerical model consists of a 2D plane strain explicit Lagrangian orthogonal cutting model developed with the

Table 2 Cutting conditions of the experiments

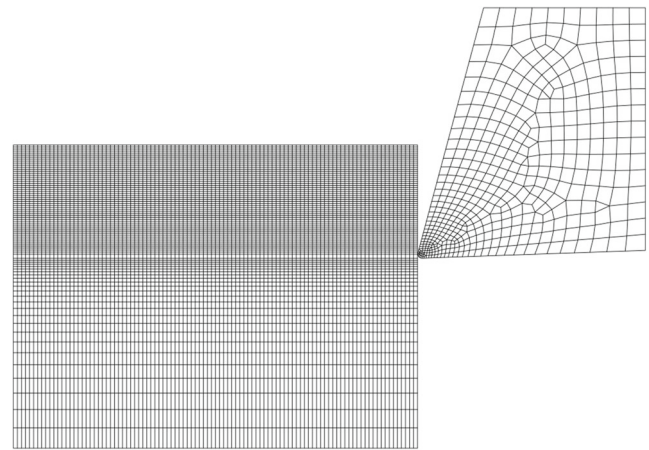|	
Cutting speed (m/min)	30
Uncut chip thicknesses (μm)	280, 100, 60, 40
Width of cut (mm)	1
Length of cut (mm)	10
Rake angle (°)	15
Clearance angle (°)	2
Cutting edge radius (μm)	10

Fig. 3 Mesh topology

commercial software ABAQUS/Explicit v6.14-2. Similarly to the current literature, it models the area close to the cutting edge of the tool. The workpiece is modeled as a rectangular block of 1 mm long and 0.75 mm high; the tool has the same geometry as for the experiments. These two parts are meshed with four-node CPE4RT linear elements (the model is composed of nearly 8500 elements). Figure 3 presents the structured mesh grid of the model at the beginning of the cut. Elements of 10 μm × 5 μm are used to mesh the chip, while rectangular elements of increasing length when moving away from the cutting region are adopted for the area under the chip. The sacrificial layer (cf. 2) is composed of square elements of 10 μm side (i.e. the cutting edge radius value). The workpiece is fixed in space while the tool moves horizontally at the cutting speed (30 m/min).

The workpiece material, *Ti6Al4V*, is assumed to be homogeneous. It is described by four different empirical constitutive models, detailed in the next paragraph. The tool material, tungsten carbide, is also homogeneous and is described by a linear elastic model. Coulomb's friction is used to model friction at the tool – chip interface with a low coefficient value (0.05) in accordance with Bäker et al. [16] and Calamaz et al. [4]. Although tool – chip contact is a key parameter in cutting, in this paper, the Coulomb model approach, one of the most used models (in Arrazola and Özel [17], Mabrouki et al. [18] for example), is considered in order to focus the attention on the material constitutive model and as qualitative information is sought. All the friction energy is converted into heat and this heat flows equally to the workpiece and the tool (classic assumptions [17, 19]). Contact heat transfer is allowed at the tool – chip interface. The heat conduction coefficient (Table 3) was chosen to reach quickly thermal steady-state thanks to the rapid temperature rise in the tool, while providing a temperature discontinuity between the chip and the tool

Table 3 Material properties and cutting conditions of the numerical model [4, 13, 15, 20, 21]

Density (kg/m^3)	Ti6Al4V	4430
	Carbide	15,000
Young's modulus (GPa)	Ti6Al4V	113.8
	Carbide	800
Expansion (K^{-1})	Ti6Al4V	8.6 e^{-6}
	Carbide	4.7 e^{-6}
Conductivity (W/mK)	Ti6Al4V	7.3
	Carbide	46
Specific heat (J/KgK)	Ti6Al4V	580
	Carbide	203
Inelastic heat fraction	Ti6Al4V	0.9
T_{melt} (K)	Ti6Al4V	1878
T_{room} (K)		298
Friction coefficient		0.05
Friction energy to heat (%)		100
Heat partition to part (%)		50
Thermal conductance (W/m^{2}K)		1,000,000
Cutting speed (m/min)		30
Uncut chip thicknesses (μm)	280, 100, 60, 40	
Rake angle (°)		15
Clearance angle (°)		2
Cutting edge radius (μm)		10

as the heat transfer is not perfect. The workpiece and tool initial temperature is set to 25°C (298 K).

Constitutive models

Four empirical constitutive models are considered in this work to represent the behavior of *Ti6Al4V*. It is important to mention that no information on the material state and treatments is provided by the authors in the papers introducing these models. The identification of the material parameters may therefore have been carried out on a material with a different metallurgical state.

The first constitutive model is the Johnson-Cook (JC) model, the most adopted model in machining modeling. The flow stress depends on strain, strain rate and temperature. It is described by three multiplicative distinctive terms. They represent, respectively, the strain hardening, the strain rate hardening and the thermal softening behaviors of the material [22]:

$$\sigma = \left[A + B\, \varepsilon^n \right] \left[1 + C\, \ln \frac{\dot{\varepsilon}}{\dot{\varepsilon}_0} \right] \left[1 - \left(\frac{T - T_{room}}{T_{melt} - T_{room}} \right)^m \right] \tag{1}$$

Where T_{melt} is the melting temperature of the workpiece material, T_{room} is the room temperature, ε is the plastic strain, $\dot{\varepsilon}$ is the plastic strain rate and $\dot{\varepsilon}_0$ is the reference plastic strain rate. Material constant A is the yield strength, B is the hardening modulus, C is the strain rate sensitivity, m is the thermal softening exponent and n is the strain-hardening exponent. Table 4 gives the set used for this study. According to Meyer and Kleponis [23], the parameters were determined at strain rate levels of 0.0001 s^{-1}, 0.1 s^{-1} and 2150 s^{-1} and at a maximum plastic strain of 0.57. Many sets leading to very different stress – strain evolutions are available in the literature [24]. These JC parameters were chosen as the value of parameter A, 862.5 MPa, is equal to the yield stress of *Ti6Al4V* at room temperature [23], which is consistent with the description of the Johnson-Cook constitutive model. It was furthermore estimated as the most popular and frequently found in literature. The main drawbacks of JC flow stress are its inability to represent high strain behavior and the uncoupled effect of strain, strain rate and temperature [7].

The second flow stress model is the TANgent Hyperbolic (TANH), which is a JC model modified by Calamaz et al. [4] to take into account the strain softening phenomenon that would be necessary to produce segmented *Ti6Al4V* chips. Indeed, according to Calamaz et al. [4], the JC model correctly represents the behavior of *Ti6Al4V* up to

Table 4 Parameters of the four empirical constitutive models [4, 6, 7, 23]

JC model			
A (MPa)	862.5		
B (MPa)	331.2		
C	0.012		
m	0.8		
n	0.34		
TANH model			
A (MPa)	968	a	1.6
B (MPa)	380	b	0.4
C	0.0197	c	6
m	0.577	d	1
n	0.421		
TANH2 model			
A (MPa)	870	q	5
B (MPa)	990	p	0.6
C	0.011	T_{rec} (K)	600
m	1	ε_0	0.7
Sima model			
A (MPa)	724.7	e	2
B (MPa)	683.1	f	5
C	0.035	g	1
m	1	h	1
n	0.47	r	0.05

strain rates of 1000 s^{-1} and strains of about 0.3. These values are smaller than what is encountered in machining: strain can be as large as 6 and strain rates as 10^7 s^{-1} [3]. Moreover strains larger than 0.5 would lead to the strain softening phenomenon, which was identified in the literature as one of the causes responsible for the formation of segmented $Ti6Al4V$ chips [9]. The physical phenomena at the origin of this strain softening are not known yet but dynamic recrystallisation (mainly in the β phase field) could be the main reason according to Ding et al. [25]. The strain softening is taken into account via the fourth term introducing the tangent hyperbolic function [4]:

$$
\sigma = \left[A + B\,\varepsilon^n \left(\frac{1}{\exp\left(\varepsilon^a\right)} \right) \right]
$$
$$
\left[1 + C\,\ln\frac{\dot{\varepsilon}}{\dot{\varepsilon}_0} \right] \left[1 - \left(\frac{T - T_{room}}{T_{melt} - T_{room}} \right)^m \right]
$$
$$
\left[E + (1 - E)\tanh\left(\frac{1}{(\varepsilon + S)^c} \right) \right] \tag{2}
$$

with

$$
E = 1 - \left(\frac{T}{T_{melt}} \right)^d \quad \text{and} \quad S = \left(\frac{T}{T_{melt}} \right)^b
$$

Parameters A, B, C, m and n have the same meaning as for JC, while a, b, c and d are new ones introduced by TANH. Parameters a and c modify the slope of the stress drop, a at high strain and c at low strain. The maximal stress value is controlled by b. Parameter d influences the magnitude of the strain softening: a high value gives a weak strain softening. The decrease of the maximal stress value when temperature increases is taken into account by S, which depends on the temperature. The introduction of the tangent hyperbolic does not alter stresses at low strains (corresponding to experimental values) and adds softening at high strains. The set of parameters of the TANH model comes from Calamaz et al. [4] and is given in Table 4.

The third constitutive model is a second version of TANH, called TANH2 in this article. According to Calamaz et al. [6], it improves the first TANH formulation in the sense that the strain softening appears from approximately T_{rec} (approximately 30% of the melting temperature) and not at room temperature anymore, as shown by experimental results reported by Calamaz et al. [6]. This law is expressed as [6]:

$$
\sigma = \left[A + B\,\varepsilon^n \right] \left[1 + C\,\ln\frac{\dot{\varepsilon}}{\dot{\varepsilon}_0} \right] \left[1 - \left(\frac{T - T_{room}}{T_{melt} - T_{room}} \right)^m \right]
$$
$$
\left[F + (1 - F)\tanh\left(\frac{1}{\varepsilon + \varepsilon_0} \right) \right] \tag{3}
$$

with

$$
F = 1 - \left[\frac{p\,\varepsilon}{1 + p\,\varepsilon} \tanh\left(\frac{T - T_{room}}{T_{rec} - T_{room}} \right)^q \right] \tag{4}
$$

By comparison with TANH, the parameter F (4) now depends on strain and temperature to better describe the strain softening phenomenon. The parameters adopted (Table 4) come from Calamaz et al. [6]. The slope of the curve after the maximal stress is controlled by parameter p. The onset temperature for the strain softening phenomenon is T_{rec} and parameter q influences the temperature range affected by the strain softening. The additional parameters, by comparison with JC, of both TANH models were obtained by Calamaz et al. through inverse analysis based on experimental cutting results.

The fourth model is another modification of TANH by Sima and Özel [7] (called Sima flow stress in this article). This consists of a TANH model with a better control on the thermal softening trough tangent hyperbolic function [7]:

$$
\sigma = \left[A + B\,\varepsilon^n \left(\frac{1}{\exp\left(\varepsilon^e\right)} \right) \right]
$$
$$
\left[1 + C\,\ln\frac{\dot{\varepsilon}}{\dot{\varepsilon}_0} \right] \left[1 - \left(\frac{T - T_{room}}{T_{melt} - T_{room}} \right)^m \right]
$$
$$
\left[G + (1 - G)\left\{ \tanh\left(\frac{1}{(\varepsilon + R)^g} \right) \right\}^r \right] \tag{5}
$$

with

$$
G = 1 - \left(\frac{T}{T_{melt}} \right)^h \quad \text{et} \quad R = \left(\frac{T}{T_{melt}} \right)^f
$$

The parameters of this constitutive model (Table 4) are given by Sima and Özel [7]. The strain hardening is controlled by parameter e by decreasing the flow stress after a critical strain value. The parameter f controls the temperature-dependent softening and at which the maximum stress occurs. Parameter h has a strong impact on the stress value and sets its minimum. Parameters g and r have interacting but similar effects on the stress. With f, g, h, the parameter r controls the $tanh$ function in thermal softening at elevated strains and temperatures. It also influences the softening trend. The TANH, TANH2
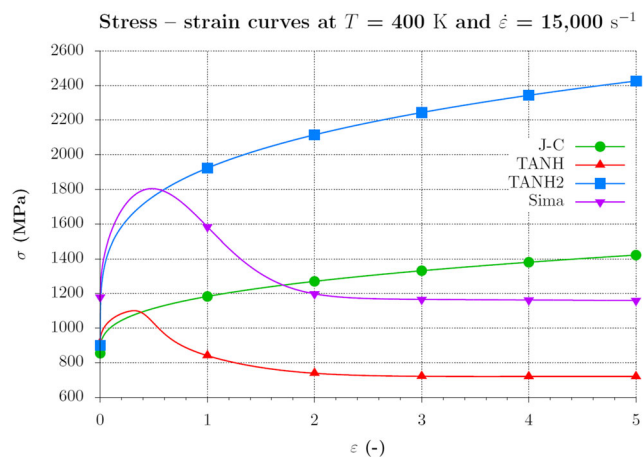

Fig. 4 Flow stress curves at 400 K and 15,000 s^{-1}

and Sima models were introduced in Abaqus in the form of a table linking the stress, the strain, the strain rate and the temperature.

The four constitutive models are plotted at a strain rate of 15,000 s^{-1} and a temperature of 400 K (below T_{rec} = 600 K) in Fig. 4 and a temperature of 800 K (above T_{rec}) in Fig. 5. When the temperature is higher (Fig. 5), lower stresses are observed, as expected due to the thermal softening. JC and TANH2 flow stresses are similar under T_{rec}, although the stress magnitude is different. Above T_{rec}, the strain softening effect is activated for TANH2 model; its shape is however different from TANH and Sima models as the stress decrease is more progressive. The shapes of TANH and Sima flow stresses are quite close to each other, the main difference being the magnitude of the stresses and the strain softening occurring at lower strain for TANH. The comparison between JC and TANH models at 400 K clearly shows the influence of the strain softening on the level of the stresses. They are close to each other at very low strains, then the difference increases with strain due to the strain softening. A similar observation is made for TANH2 and Sima models: stresses are close at low strain and differ at high strains. This difference decreases when strain increases for temperature above T_{rec}. Two groups can be made based on the stress magnitude before the activation of strain softening (i.e. at low strain): JC and TANH on one hand and TANH2 and Sima on the other hand. This difference in the stress magnitude is mainly due to the large difference in the value of parameter B.

To conclude on the constitutive models, different cutting forces magnitudes can be expected as different stresses levels are noted. The shapes of the flow stresses should also influence the chips morphologies. The differences of the JC parameters among the four models are quite significant. Figures 4 and 5 clearly show that there is a need to specify the state of the material in future research aiming at the identification of material models
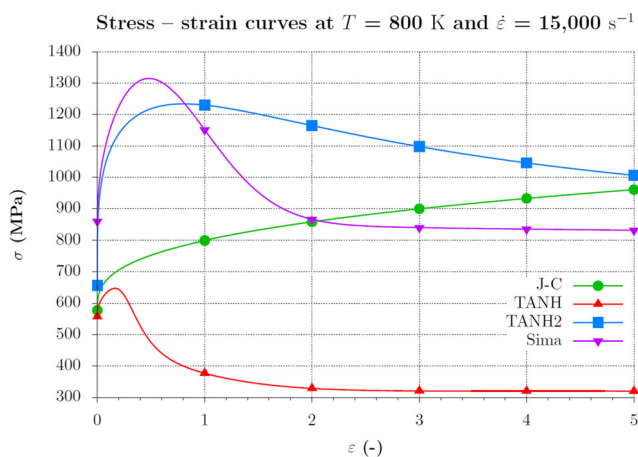
parameters. Current available information may lead to the comparison of materials with different metallurgical state inducing differences in the results. The need to specify the metallurgical state of the material when identifying the parameters of the constitutive model has already been mentioned in the particular case of the Johnson-Cook model [24]. For TANH, TANH2 and Sima constitutive models, less different sets of parameters are available in the literature than for JC model. The values of the parameters used in this study come from the articles introducing these three models, Calamaz et al. [4], Calamaz et al. [6] and Sima and Özel [7], respectively. This allows to reach the goal of the current study: assessing the performance of each constitutive model with the "original" set of parameters with which it was developed and comparing them with the reference model of Johnson-Cook.

Material damage modeling

Due to the Lagrangian formulation, a chip separation criterion is needed to allow the chip formation. An "eroding" element criterion based on crack propagation depending on the stress and strain state of the machined material is adopted. This chip formation approach, by ductile failure phenomenon, is in agreement with the experimental findings of Subbiah and Melkote [26]. It is composed of two steps. In the first one, a damage initiation criterion must be fulfilled. The second step concerns damage evolution, based on the fracture energy approach. This kind of chip formation modeling has been introduced by Mabrouki et al. [27] for AISI 4340 and the ALE formalism. Mabrouki et al. [28] then modified the workpiece geometry to introduce a chamfer and reduce the mesh distortion and optimize contact management for Al2024-T351. Mabrouki et al. [18], Zhang et al. [29] and Chen et al. [30] adopted the same model for *Ti6Al4V* with the Johnson-Cook constitutive model (without chamfer on the workpiece for Chen et al. [30]).

The damage initiation criterion is the Johnson-Cook shear failure model [31]. The initiation of damage is computed in each element by

$$\omega = \sum \frac{\Delta \varepsilon}{\varepsilon_{D=0}} \tag{6}$$

In which $\Delta \varepsilon$ is the increment of equivalent plastic strain, $\varepsilon_{D=0}$ is the equivalent plastic strain when damage is initiated ($\omega = 1$). It is computed with the Johnson-Cook shear failure model [31]:

$$\varepsilon_{D=0} = \left[D_1 + D_2 \, \exp\left(D_3 \, \sigma^*\right) \right] \left[1 + D_4 \, \ln \frac{\dot{\varepsilon}}{\dot{\varepsilon}_0} \right]$$
$$\left[1 - D_5 \left(\frac{T - T_{room}}{T_{melt} - T_{room}} \right) \right] \tag{7}$$

Fig. 5 Flow stress curves at 800 K and 15,000 s^{-1}

Table 5 Johnson-Cook failure model parameters [32]

Parameter	Value
D_1	–0.09
D_2	0.27
D_3	0.48
D_4	0.014
D_5	3.87

With $\sigma^* = \frac{\sigma_m}{\sigma}$ the stress triaxiality, σ_m the mean stress and σ the equivalent Von Mises stress. Variables D_1 to D_5 are the shear failure model parameters and the other variables have the same meaning as for the Johnson-Cook flow stress model. Their values are given in Table 5.

In order to reduce the mesh dependence to localization during damage evolution (after the damage initiation criterion has been reached), fracture energy during crack propagation [33], G_f, is introduced to represent the stress-displacement relation rather than the stress-strain relation:

$$G_f = \int_{\varepsilon_{D=0}}^{\varepsilon_{D=1}} L_c \, \sigma \, \mathrm{d}\varepsilon = \int_0^{u_{D=1}} \sigma \, \mathrm{d}u \tag{8}$$

With L_c the element characteristic length and u the equivalent displacement. Before the onset of damage, $u = 0$ and after, $u = L_c \varepsilon$. The element characteristic length depends on the element geometry. For plane elements, it is defined as the square root of the element surface [34]. The fracture energy G_f is the required energy to open a unitary area crack. In plane strain, it is given by

$$G_f = \frac{1 - \nu^2}{E} K_C^2 \tag{9}$$

Where ν is Poisson's ratio, E is Young's modulus, K_C is fracture toughness in mode I (K_{IC}) [35]. The evolution of damage, D, can be either linear

$$D = \frac{L_c \, \varepsilon}{u_{D=1}} = \frac{u}{u_{D=1}} \tag{10}$$

either exponential

$$D = 1 - \exp\left(-\int_0^{u_{D=1}} \frac{\sigma}{G_f} \, \mathrm{d}u\right) \tag{11}$$

The value of D goes from 0 when damage is initiated (and $\omega = 1$) to 1 at material failure. As soon as the specified value of G_f is reached in a finite element, it is deleted and all of its stress components are put to zero. The suppression of a finite element introduces a crack in the workpiece, making it possible for the chip to come off. In this model, the chip separation is assumed to occur along a predefined straight path composed of one element in height. Damage properties with linear evolution [18, 29] are therefore given only to this part of the workpiece, typically called "sacrificial layer" [26] (or "separation line" [30]), in a first time to allow the comparison of the four constitutive models. Damage will be introduced in the chip in a second time to obtain a more realistic segmented morphology.

Segmented chip formation with the four constitutive models without damage in the chip

The experimental chips were collected before being embedded into epoxy resin to stand on their edge and polished straight across their length. To characterize the segmented chip geometry, four lengths (highlighted in

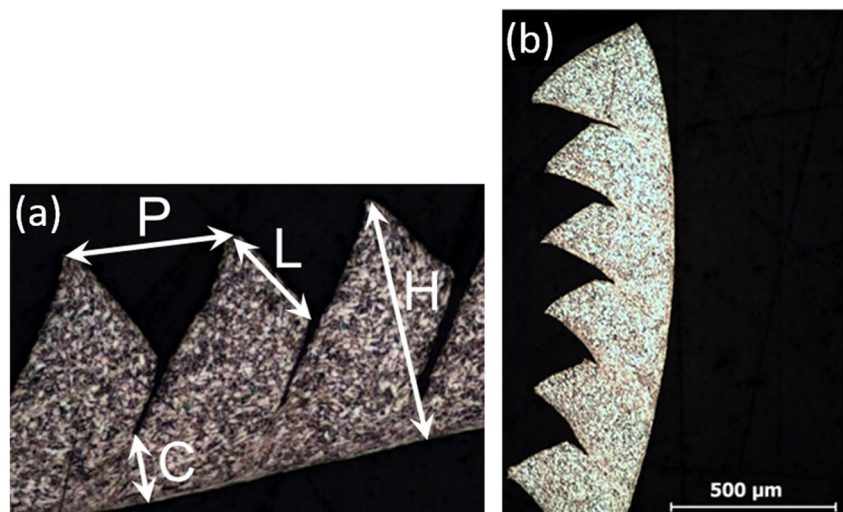**Fig. 6 a** Characteristic lengths of a segmented chip [13], **b** Experimental chip at $h = 280$ μm [13]

Fig. 7 Numerical chips at $h =$ 280 μm without damage in the chip after 600 μs **a** JC, **b** TANH, **c** TANH2 and **d** Sima, temperature plots (in K)
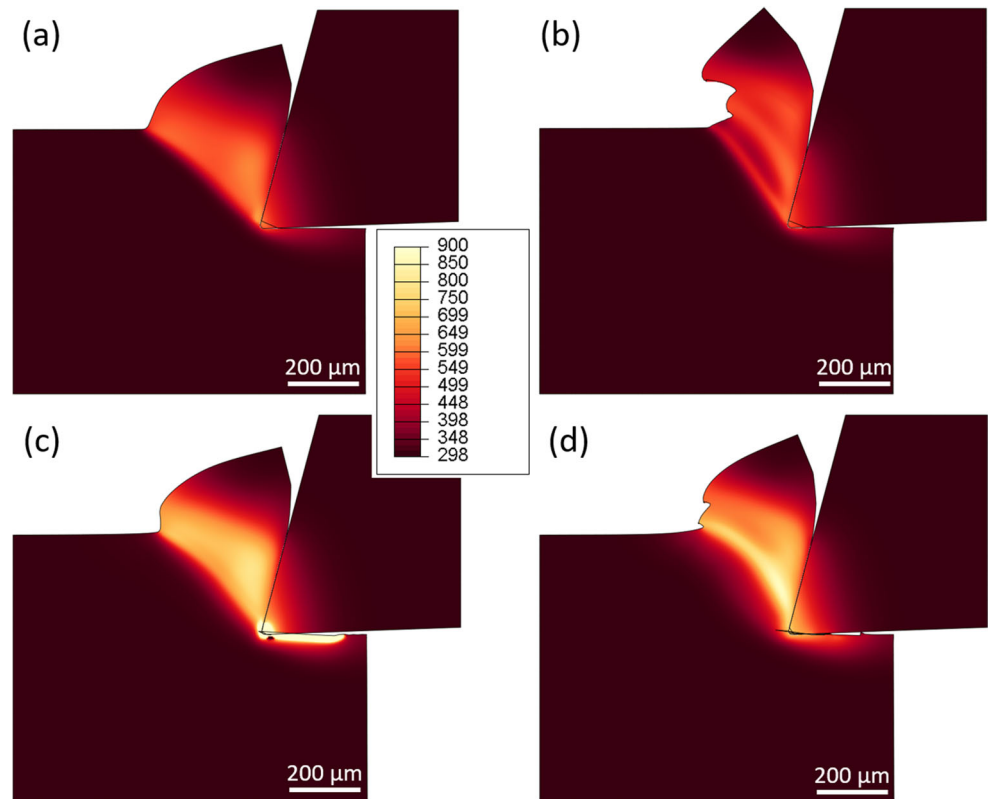

Fig. 6a) are usually measured [36]: the undeformed segment length L, the height of the segment H, the valley C and the pitch P. The mean values (on 25 segments) of these characteristic lengths are given in Table 7.

At this stage, the objective is to highlight the differences resulting of only the constitutive models and so no damage properties are given in the chip. The four numerical chips are shown in Fig. 7 after 600 μs of simulation (the steady state for the cutting force and the chip thickness is reached after 200 μs for the modeling). It is clear that they are all far away from the experimental one: none has the geometry of a segmented chip as experimentally observed. It consequently does not make sense to measure their characteristic lengths when looking at the chips morphologies in Figure 7 (continuous or slightly segmented chips). Some differences between the chips are however observed. The chips from JC and TANH2 flow stresses are continuous, while they have small segments with TANH and Sima models. The chip morphology with Sima model is more regular than with TANH for which the first segment is more marked (its valley is lower). From the morphology point of view, these four constitutive models do therefore not allow to form a satisfactory chip.

Differences are also noted on the cutting forces evolutions plotted in Fig. 8 for each numerical case together with the experimental values. These differences are of two types: the shape of the evolution and the magnitude. Two

shapes are observed in Fig. 8: nearly constant and with oscillations around a mean value. The forces evolutions are closely linked to the chip morphology. Indeed, the cutting force is nearly constant when the chip is continuous and has a cyclic evolution in regime when it is slightly segmented: the evolutions of the cutting force for JC and TANH2 models are nearly constant and the chips are continuous, while small segments are observed for the two others and
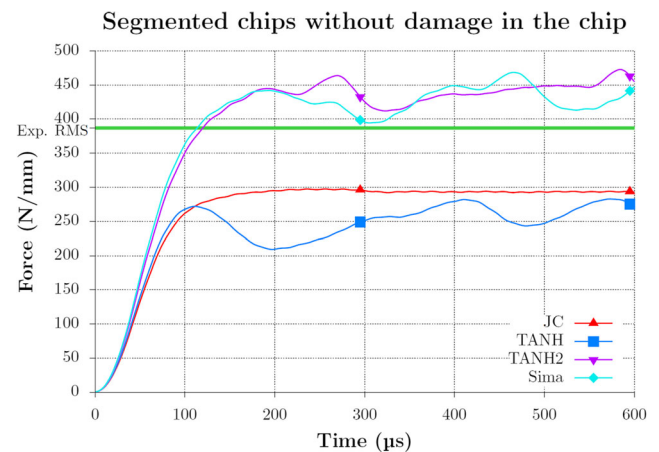

Fig. 8 Comparison of the numerical cutting forces with the experimental RMS value (the thickness of the experimental line represents the standard deviation) at $h = 280$ μm without damage in the chip, low-pass filter cutoff frequency at 10 kHz

Table 6 RMS cutting forces values at $h = 280$ μm, closest values to experimental reference in bold

	Fc [N/mm]	Fc with dam. [N/mm]
Experiment [13]	387 ± 2	387 ± 2
JC	292	254
TANH	255	220
TANH2	442	**301**
Sima	**432**	**301**

Table 7 Characteristic lengths with damage in the chip at $h = 280$ μm (L: undeformed segment length, H: height of the segment, C: valley and P: pitch, experimental measurements on 25 segments), closest values to experimental reference in bold

	L [μm]	H [μm]	C [μm]	P [μm]
Exp. [13]	206 ± 17	288 ± 14	157 ± 21	233 ± 17
JC	–	–	–	–
TANH	94 ± 5	252 ± 2	**181 ± 4**	110 ± 10
TANH2	152 ± 4	303 ± 2	59 ± 11	82 ± 2
Sima	**153 ± 11**	**290 ± 4**	74 ± 22	92 ± 8

their cutting force is not constant anymore. The magnitude of the forces is closely linked to the flow stress: when the level of the stresses is higher, the magnitude of the cutting force is higher as well. The root mean square (RMS) values of the cutting forces (Table 6) confirm it and clearly show that the lower stresses of JC and TANH models result in lower cutting forces than TANH2 and Sima models. Looking back at Fig. 4, it becomes obvious that the absence of small segments in the chip is due to the strain softening not taken into account in the constitutive law or to the temperature too low to activate it (Fig. 5). Table 6 shows that Sima flow stress gives the closest RMS cutting force value to the experiments, with a difference of 12% with the experimental reference.

To conclude this paragraph, the numerical results so far exhibit significant differences with the experiments; the main one being the modeled chips morphologies far from the experimental one. As stated previously, the objective was to compare the four different constitutive models and their ability to produce a realistic chip without damage properties in the chip to provide information related only to the constitutive model. The significant chips morphologies differences mean that, for the cutting conditions adopted, the considered flow stresses alone do not allow to produce a satisfactory chip. TANH and Sima models give results closer to the experiments than JC and TANH2 models but the differences are however significant. Previous experimental [13, 37] and numerical [4, 9] works on *Ti6Al4V* segmented chips formation showed that a crack propagates inside the primary shear zone and that it should be taken into account to form a chip with a morphology close to the experiments. Damage will accordingly be introduced in the chip.

Inclusion of damage in the chip with the four constitutive models

To model crack propagation in the primary shear zone when a segmented chip is formed, damage is introduced the same way in the chip as in the sacrificial layer:

Johnson-Cook damage failure in two steps is used with an exponential evolution of damage parameter D [18, 28]. Figure 9 shows the corresponding four numerical chips after 1350 μs of simulation. More than 600 μs are modeled with damage in the chip in order to have enough segments to measure the characteristic lengths of the chips on more than one segment. All of the chips are different from these without damage and none is continuous anymore. The three chips with a constitutive model taking strain softening into account now exhibit a segmented morphology. With TANH2 and Sima flow stresses, the chips are qualitatively very close. Such a chip with TANH2 model was not expected when looking back at the results without damage. That morphology change is due to the larger deformation in the primary shear band involved by the crack propagation. It induces an increase of the temperature above T_{rec} in the primary shear zone, turning on the strain softening. These chips are now closer to the experimental reference (Figure 6 (b)).

The characteristic lengths of the segmented chips are given in Table 7. To avoid the influence of a difference in the results between the modelling and the experiments due to the different cutting times (leading to differences in the cutting process and therefore the chip geometry and cutting forces), the same portion of the chip is considered. As can be seen in Fig. 6b, only the first segments of the chip (i.e. where the cutting process is starting) are considered, which is consistent with Fig. 9. The very first segment of each chip is not taken into account as the tool has just entered into the workpiece. The chip with the closest lengths to the experiments is that with Sima model. The undeformed segment length is still underestimated (and equal to that with TANH2 model), while the height of the segments is very close to the experiments; they can be considered as equal due to the standard deviations. The valley is nearly half that of the reference one, indicating that the crack propagates too easily in the primary shear zone. This is even worse with TANH2 model, contrary to the too large, but closer to the experiments, TANH valley. Such a small valley leads to a

Fig. 9 Chips at h = 280 μm with damage in the chip after 1350 μs **a** JC, **b** TANH, **c** TANH2 and **d** Sima, temperature plots (in K)
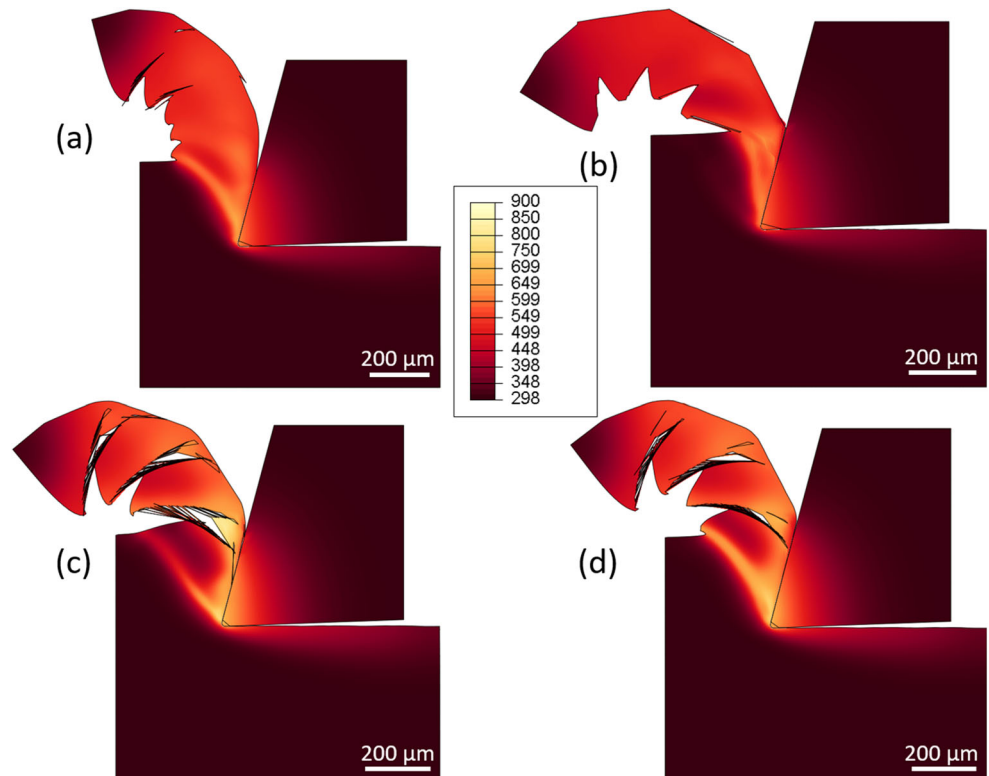
chip with a low rigidity. Self-contact is not enabled in the model, emphasizing the rolling of the chip on itself. The values of the pitch are therefore only indicative and will not be used in the comparison. It is however not surprising to note that the pitch of the chip with TANH model is larger than with TANH2 and Sima models as its valley (and thus rigidity) is larger.

In Fig. 10, it is seen that none of the cutting forces evolutions is constant anymore, in accordance with the
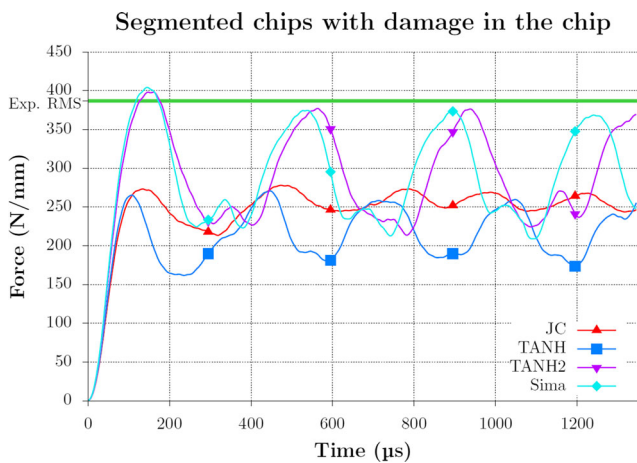
Fig. 10 Comparison of the numerical cutting forces with the experimental RMS value (the thickness of the experimental line represents the standard deviation) at h = 280 μm with damage in the chip, low-pass filter cutoff frequency at 10 kHz

chips morphologies. They can be linked to the segments formation: a decrease in the force corresponds to the formation of a segment and the magnitude of the force variation is the image of the size of the segments. This is an important qualitative information, coupled with the capacity of the model to produce realistic segmented chips qualitatively close to the experimental reference. As previously, two levels of magnitude are observed: low with JC and TANH models and high with TANH2 and Sima models, which is confirmed by the RMS values presented in Table 6. The numerical forces are lower than without damage in the chip due to the oscillations caused by the formation of the segments and the larger width of the valleys of the cutting forces, leading to a decrease of the RMS values. All of them are now lower than the experimental reference. The constitutive models leading to the closest cutting forces are Sima and TANH2 with values exhibiting a difference of 22% by comparison with the experimental reference. The addition of damage in the chip therefore brings the morphology close to that of the experiments, while it degrades the prediction of the cutting force RMS value.

The segmentation frequency, f_g is computed from the undeformed segment length, L, and the cutting speed , V_c by [38]:

$$f_g = \frac{V_c}{L} \tag{12}$$

The experimental segmentation frequency is 2427 Hz. The numerical model with Sima flow stress has a segmentation frequency of 3268 Hz. By comparison, the TANH constitutive model leads to a frequency of 5319 Hz. The difference with the experimental value is larger, which was expected as the undeformed segment length is smaller and the frequency of the cutting force variations (Fig. 10) is higher. Moreover, after the same cutting length, more segments are formed with TANH constitutive model by comparison with Sima's (Fig. 9b and d).

To conclude on the comparison of the four empirical constitutive models considered, the results on the chips morphologies and on the cutting forces show that the closest geometry and the closest RMS value of the cutting force are obtained with Sima flow stress. It is therefore the most suited model to represent *Ti6Al4V* in machining modeling for the cutting conditions adopted in this study. The comparison with the results without damage in the chip clearly shows that similar trends are obtained for the forces which, in addition to the prediction of segmented chips morphologies, confirms the capacity of the model to correctly predict the trends and give relevant qualitative information. In accordance with previous works [4, 9, 13, 37], the results show that *Ti6Al4V* segmented chip formation

is due to the strain softening and the propagation of a crack inside the primary shear zone.

Application to continuous chips formation

The main objective of the numerical model is to predict the trend of the results evolution when the cutting conditions vary. Up to now, only one uncut chip thickness has been considered, 280 µm, that lead to the formation of a segmented chip. The three other uncut chip thicknesses of the experiments (40 µm, 60 µm and 100 µm) gave continuous chips [13]; all the other cutting conditions (Table 2) are unchanged. The three experimental chips are shown in Fig. 11a to c at a magnification factor of 200. They consist of continuous chips with very small and irregular segments along their entire length. No cracks were observed at these uncut chip thicknesses. Again, the chips were not deformed during the unrolling preceding the embedding thanks to the small cutting length (10 mm), providing short and not rolled up chips. The characteristics of the finite element model are the same as in the previous paragraph: the Sima constitutive model is adopted with damage in the sacrificial layer and in the chip. Only the
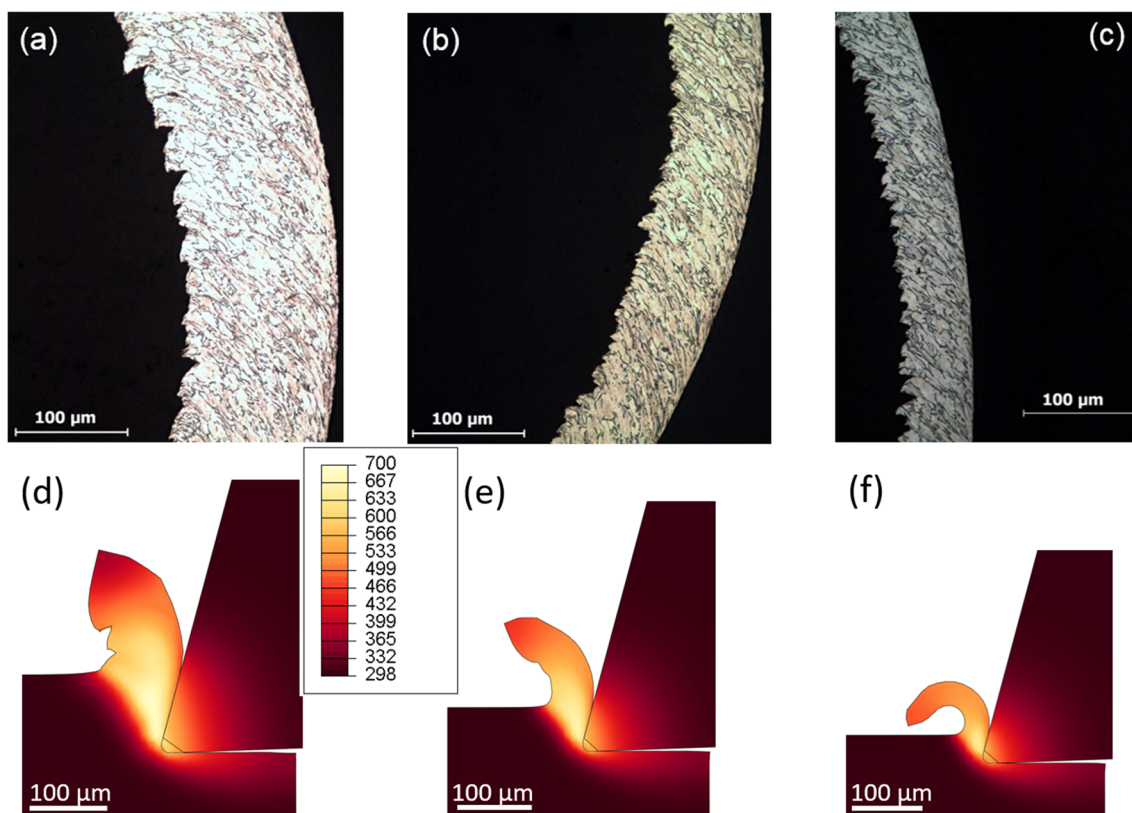

Fig. 11 Experimental [13] **a** 100 µm, **b** 60 µm, **c** 40 µm and numerical chips (Sima model with damage in the chip) after 350 µs **d** 100 µm, **e** 60 µm, **f** 40 µm, temperature plots (in K)
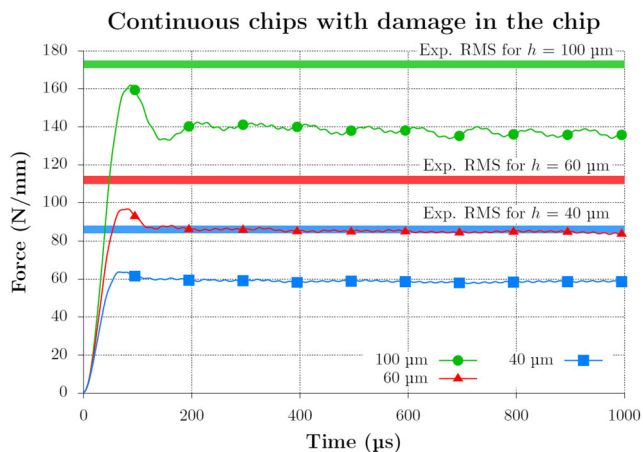
Fig. 12 Comparison of the numerical cutting forces (Sima model with damage in the chip) with the experimental RMS values (the thickness of the experimental lines represents the standard deviation) at $h = 100$ μm, 60 μm and 40 μm, low-pass filter cutoff frequency at 10 kHz

Table 8 Cutting forces (Sima model with damage in the chip) summary when the chips are continuous

h (μm)	Exp. [13] (N/mm)	Sim. (N/mm)
100	173 ± 2	139
60	112 ± 2	86
40	86 ± 2	59

the numerical RMS value is lower than the experimental reference. The difference is between 20% and 30%, which is accurate enough to predict evolution trends for different cutting conditions. This shows that these other cutting conditions are well handled by the model and confirms the choice of Sima constitutive model.

Conclusions

Four empirical constitutive models aimed for modeling of *Ti6Al4V* in machining operation were considered. This study showed that they had a strong influence on the chip formation and the magnitude of the cutting force. Significant differences in the JC parameters of the four constitutive models were highlighted. They lead to differences in the stress-strain evolutions and in the cutting forces. The absence of information on the material used for the parameters identification may be the reason: different metallurgical states will induce different material behaviors and then different constitutive model parameters. It is therefore recommended to specify this information in future research focusing on the identification of material models parameters. The absence of damage properties in the chip showed the specificities of each flow stress but they were not sufficient, in these cutting conditions, to form a segmented chip close to the experimental reference. It was shown that the strain softening and the crack propagation in the chip are necessary features to form a segmented chip with a morphology close to the experimental reference.

Although some differences were still noticed for the morphology, as well as for the cutting force, in the cutting conditions adopted in this paper, the Sima constitutive model lead to the closest results to the experiments. The difference in the cutting force with the experimental reference value is of 22%, while, for the chip morphology, it is less than 1% for the height of the segments, 25% for the undeformed segment length and 53% for the valley. The application of the same finite element model (Sima constitutive model with crack propagation in the chip) for other uncut chip thicknesses values confirmed that it was well suited to model *Ti6Al4V* orthogonal cutting. The numerical morphologies were close to the experimental tests and it is important to note that, although crack propagation

uncut chip thickness is modified to correspond to that of the experiments.

The three numerical chips (Fig. 11d to f) are continuous as in the experimental reference, showing the ability of the model to give accurate results for different cutting conditions. To quantitatively characterize the chip morphologies, their thickness, h', could have been measured. However, due to the sacrificial layer in the numerical model, a significant amount of material is lost when the uncut chip thickness is small (about 10% at 100 μm, 17% at 60 μm and 25% at 40 μm) and it makes no sense to measure it for a quantitative comparison with the experiments. Small segments qualitatively close to the experiments are observed for an uncut chip thickness of 100 μm. The numerical chips at 60 μm and 40 μm do not have these small segments (likely due to a mesh size larger than these very small segments). They tend to roll up after a small length of cut, contrary to the experiments. Modeled chips less rigid than the experimental ones were already observed at the uncut chip thickness of 280 μm. Although crack propagation in the chip is enabled in the numerical model, no crack is noticed. This is consistent with the experimental observations and confirms that the finite element model is well suited for *Ti6Al4V* orthogonal cutting modeling in different cutting conditions leading to different chip morphologies.

The chip is continuous for the three uncut chip thicknesses and therefore the cutting force (Fig. 12) is nearly constant and present small oscillations, as expected. At the beginning of the cut, a peak in the cutting force is clearly observed for the modeling. Its magnitude decreases with the uncut chip thickness. Table 8 summarizes the average RMS values of the forces for each cutting condition. As expected, the lower the uncut chip thickness, the lower the level of the forces. As for the uncut chip thickness of 280 μm,

is enabled, no crack is observed in the chips at these smaller uncut chip thicknesses. This is in accordance with the experiments and highlights the ability of the model to produce reliable chips morphologies. The cutting force was estimated with an average error of 25%.

These results show that the model is able to give good results even with changing cutting conditions and in particular that the chip morphology changes completely in accordance with the experiments, without any tuning of the model. The presented model with the Sima flow stress and damage in the chip is therefore able to predict different types of chip morphologies (segmented, continuous) and to give relevant quantitative information, such as the cutting force, for different cutting conditions.

Compliance with Ethical Standards

Conflict of interests The authors declare that they have no conflict of interest.

References

1. Destefani J (1990) Introduction to titanium and titanium alloys, properties and selection: nonferrous alloys and special-purpose materials, vol 2. ASM Handbook
2. Lee W, Lin C (1998) High-temperature deformation behaviour of Ti6Al4V alloy evaluated by high strain-rate compression tests. J Mater Process Technol 75:127–136
3. Pantalé O (2005) Plateforme de prototypage virtuel pour la simulation numérique en grandes transformations thermomécaniques rapides. Tech. rep. Institut National Polytechnique de Toulouse
4. Calamaz M, Coupard D, Girot F (2008) A new material model for 2D numerical simulation of serrated chip formation when machining titanium alloy Ti-6Al-4V. Int J Mach Tools Manuf 48:275–288
5. Calamaz M, Coupard D, Nouari M, Girot F (2011) Numerical analysis of chip formation and shear localisation processes in machining the Ti-6Al-4V titanium alloy. Int J Adv Manuf Technol 52:887–895
6. Calamaz M, Coupard D, Girot F (2010) Numerical simulation of titanium alloy dry machining with a strain softening constitutive law. Mach Sci Technol 14:244–257
7. Sima M, Özel T (2010) Modified material constitutive models for serrated chip formation simulations and experimental validation in machining of titanium alloy Ti-6Al-4V. Int J Mach Tools Manuf 50:943–960
8. Karpat Y (2011) Temperature dependent flow softening of titanium alloy Ti6Al4V: An investigation using finite element simulation of machining. J Mater Process Technol 211:737–749
9. Ducobu F, Rivière-Lorphèvre E, Filippi E (2014) Numerical contribution to the comprehension of saw-toothed Ti6Al4V chip formation in orthogonal cutting. Int J Mech Sci 81:77–87
10. Melkote SN, Grzesik W, Outeiro J, Rech J, Schulze V, Attia H, Arrazola PJ, M'Saoubi R, Saldana C (2017) Advances in material and friction data for modelling of metal machining. CIRP Ann Manuf Technol 66:731–754
11. Ducobu F, Arrazola PJ, Rivière-Lorphèvre E, Filippi E (2015) Comparison of several behaviour laws intended to produce a realistic Ti6Al4V chip by finite elements modelling. Key Engineering Materials 651–653:1197–1203
12. Imbrogno S, Rotella G, Umbrello D (2014) On the flow stress model selection for finite element simulations of machining of ti6al4v. Key Eng Mater 611:1274–1281
13. Ducobu F, Rivière-Lorphèvre E, Filippi E (2015) Experimental contribution to the study of the Ti6Al4V chip formation in orthogonal cutting on a milling machine. Int J Mater Form 8:455–468
14. Poulachon G, Moisan A, Jawahir I (2001) On modelling the influence of thermo-mechanical behavior in chip formation during hard turning of 100cr6 bearing steel. CIRP Ann Manuf Technol 50(1):31–36
15. Lampman S (1990) Wrought titanium and titanium alloys, properties and selection: Nonferrous alloys and special-purpose materials. ASM Handbook, ASM International 2:592–633
16. Bäker M, Rosler J, Siemers C (2002) A finite element model of high speed metal cutting with adiabatic shearing. Comput Struct 80:495–513
17. Arrazola P, Özel T (2010) Investigations on the effects of friction modeling in finite element simulation of machining. Int J Mech Sci 52:31–42
18. Zhang Y, Mabrouki T, Nelias D, Gong Y (2011) FE-model for titanium alloy (Ti-6Al-4V) cutting based on the identification of limiting shear stress at tool-chip interface. Int J Mater Form 4:11–23
19. Nasr M, Ng EG, Elbestawi M (2007) Effects of workpiece thermal properties on machining-induced residual stresses - thermal softening and conductivity. Proceedings of the Institution of Mechanical EngineersPart B: Journal of Engineering Manufacture 221:1387–1400
20. Özel T, Zeren E (2007) Numerical modelling of meso-scale finish machining with finite edge radius tools. Int J Mach Mach Mater 2:451–768
21. Sun J, Guo YB (2009) Material flow stress and failure in multiscale machining titanium alloy Ti-6Al-4V. Int J Adv Manuf Technol 41:651–659
22. Johnson G, Cook W (1983) A constitutive model and data for metals subjected to large strains, high strain rates and high temperatures. Proceedings of the Seventh International Symposium on Ballistics, The Hague, The Netherlands, pp 541?547
23. Meyer HW, Kleponis DS (2001) Modeling the high strain rate behavior of titanium undergoing ballistic impact and penetration. International Journal of Impact Engineering 26:509–521
24. Ducobu F, Rivière-Lorphèvre E, Filippi E (2017) On the importance of the choice of the parameters of the Johnson-Cook constitutive model and their influence on the results of a Ti6Al4V orthogonal cutting model. Int J Mech Sci 122:143–155
25. Ding R, Guo Z, Wilson A (2002) Microstructural evolution of a Ti-6Al-4V alloy during thermomechanical processing. Mater Sci Eng A327:233–245
26. Subbiah S, Melkote SN (2008) Effect of finite edge radius on ductile fracture ahead of the cutting tool edge in micro-cutting of Al2024-T3. Mater Sci Eng A 474:283–300

27. Mabrouki T, Deshayes L, Ivester R, Rigal JF, Jurrens K (2004) Material modeling and experimental study of serrated chip morphology. Proceedings of 7th CIRP international workshop on modeling of machining operations, pp 53–66

28. Mabrouki T, Girardin F, Asad M, Rigal JF (2008) Numerical and experimental study of dry cutting for an aeronautic aluminium alloy (A2024-T351). Int J Mach Tools Manuf 48:1187–1197

29. Zhang Y, Mabrouki T, Nelias D, Gong YD (2011) Chip formation in orthogonal cutting considering interface limiting shear stress and damage evolution based on fracture energy approach. Finite Elem Anal Des 47:850–863

30. Chen G, Ren C, Yang X, Jin X, Guo T (2011) Finite element simulation of high-speed machining of titanium alloy (ti-6al-4v) based on ductile failure model. Int J Adv Manuf Technol 56:1027–1038

31. Johnson G (1985) Strength and fracture characteristics of a titanium alloy (.06ai, .04v) subjected to various strains, strain rates, temperatures and pressures. Tech. rep., NSWC TR 86-144, Dahlgren, VA

32. Bouchnak TB (2010) Etude du comportement en sollicitations extrêmes et de l'usinabilité d'un nouvel alliage de titane aéronautique: le Ti555-3. PhD thesis, Arts et Métiers ParisTech - Centre de Angers

33. Hillerborg A, Modéer M, Petersson P (1976) Analysis of crack formation and crack growth in concrete by means off racture mechanics and finite elements. Cem Concr Res 6:773–782

34. HKS (2011) Abaqus analysis user's manual, version 6.11. Dassault Systèmes

35. Henry S, Dragolich K, Dimatteo N (1995) Fatigue data book: light structural alloys. ASM International

36. Umbrello D (2008) Finite element simulation of conventional and high speed machining of Ti6Al4V alloy. J Mater Process Technol 196:79–87

37. Vyas A, Shaw MC (1999) Mechanics of saw-tooth chip formation in metal cutting. J Manuf Sci Eng 121:163–172

38. Sun S, Brandt M, Dargusch M (2009) Characteristics of cutting forces and chip formation in machining of titanium alloys. Int J Mach Tools Manuf 49:561–568